J. Fluid Mech. (2006), *vol.* 546, *pp.* 227–253. © 2005 Cambridge University Press
doi:10.1017/S0022112005007160 Printed in the United Kingdom

Experimental validation of detonation shock dynamics in condensed explosives

By DAVID E. LAMBERT[1] D. SCOTT STEWART[2], SUNHEE YOO[2] AND BRADLEY L. WESCOTT[2]

[1]Air Force Research Laboratory, Munitions Directorate, Eglin Air Force Base, FL 32542, USA
[2]University of Illinois, Urbana, IL 61801, USA

(Received 25 February 2005 and in revised form 5 July 2005)

Experiments in the HMX-based condensed explosive PBX-9501 were carried out to validate a reduced, asymptotically derived description of detonation shock dynamics (DSD) where it is assumed that the normal detonation shock speed is determined by the total shock curvature. The passover experiment has a lead disk embedded in a right circular cylindrical charge of PBX-9501 and is initiated from the bottom. The subsequent detonation shock experiences a range of dynamic states with both diverging (convex) and converging (concave) configurations as the detonation shock passes over the disk. The time of arrival of the detonation shock at the top surface of the charge is recorded and compared against DSD simulation and direct multi-material simulation. A new wide-ranging equation of state (EOS) and rate law that is constrained by basic explosive characterization experiments is introduced as a constitutive description of the explosive. This EOS and rate law is used to compute the theoretical normal shock velocity, curvature relation of the explosive for the reduced description, and is also used in the multi-material simulation. The time of arrival records are compared against the passover experiment and the dynamic motion of the shock front and states within the explosive are analysed. The experiment and simulation data are in excellent agreement. The level of agreement, both qualitative and quantitative, of theory and simulation with experiment is encouraging because it indicates that descriptions such as the wide-ranging EOS/rate law and the corresponding reduced DSD description can be used effectively to model real explosives and predict complex dynamic behaviors.

1. Introduction

Explosive systems involve an explosive charge that when ignited, propagates a detonation wave (or waves) that interacts with the working materials, i.e. the confining metals, plastics and other inert materials of the system upon which the detonation product gases do useful work in a controlled manner. Such systems form part of a basic technology that is used for military, mining and less commonly known materials processing, pulsed power and biomedical applications (Davis 1998*a*). Explosive and pyrotechnic devices are also central elements in satellite and aerospace systems. Miniaturization of explosive systems for novel application drives the search for new designs.

Advanced design of explosive systems requires a sophisticated understanding of the dynamics of condensed phase detonation. The explosive systems are designed by assuming that one or multiple detonation fronts work synchronously to generate

https://doi.org/10.1017/S0022112005007160 Published online by Cambridge University Press

precise motion and material states in the adjoining (inert) materials to produce the desired action. Conventional designs have assumed that the detonation shock propagates normal to itself at the Chapman–Jouguet (CJ) velocity. This motion rule is called the line of sight or Huygens construction. Given the motion rule and starting points for the detonation, we can propagate a front through the explosive piece and calculate the time of arrival (TOA) at the surfaces of the inert materials, that are subsequently acted on by the arriving detonation products. Calculation of the arrival time of the fronts from this simple engineering rule is almost enough to work out basic designs. However, more complex systems, such as those with multiple ignition points, smaller and complex explosive geometries, and the desire to engineer complex sequences of synchronous actions, require greater accuracy than that provided by a simple Huygens rule.

For many applications, the length of the detonation reaction zone for a steady, one-dimensional Zeldovich–von Neumann–Doering (ZND), Chapman–Jouguet wave, is a fraction of a millimetre with $\ell_{RZ} \sim O(1\,\mathrm{mm})$, or smaller so that the scale ratio of the device size to the reaction zone is huge and typically is $O(1000)$ or larger. In which case the detonation front thickness is thin relative to the geometric proportions of the engineering device. As designed systems become small, non-ideal effects associated with a finite thickness of the detonation reaction zone come directly into play as the system experiences losses. In particular, the simple Huygens motion rule neglects important reaction zone effects on the normal detonation shock speed owing to curvature of the detonation shock and unsteadiness of the detonation reaction zone.

An extensive body of theoretical and experimental work has been carried out to examine the impact of these effects on the detonation shock dynamics. The basic mathematical model for the explosive is the compressible Euler equations with a single one-step reaction from reactants to products. The explosive is represented by an $e(p, v, \lambda)$ equation of state (EOS), with p, v and λ being the pressure, specific volume and reaction progress variable and a reaction rate law $r(p, v, \lambda)$. The asymptotic theory of detonation shock dynamics (DSD) Stewart & Bdzil (1988), Bdzil & Stewart (1989), refers to hydrodynamic flow theory that corrects a planar detonation to account for changes due to the shock curvature. The theory assumes specifically that the radius of curvature of the shock is large compared to the length of the reaction zone that supports the detonation. This paper assumes the simplest reduced form that invokes only the first-order term of the asymptotic expansion. The higher-order terms of the asymptotic description capture unsteady effects of shock acceleration and their transient states. Reviews of the asymptotic theory and its application can be found in Stewart (1998) and Bdzil (2003). This paper is principally concerned with a validation of the reduced theory by comparison with appropriate experiment and direct simulation of the experiment.

The reduced detonation shock dynamics (DSD) theory assumes that lead detonation shock is weakly curved and the reaction zone is quasi-steady and derives the result that total curvature $\kappa = \kappa_1 + \kappa_2$, is a function of the normal detonation shock velocity, D_n written as

$$\kappa = F(D_n), \tag{1.1}$$

with the property $F(D_{CJ}) = 0$, where D_{CJ} is the Chapman–Jouguet velocity.

The normal shock, curvature relation is dependent on the explosive's constitutive properties and notably on the specific choice for the equation of state and reaction rate law. Experiments serve as a powerful constraint on the allowable forms for

https://doi.org/10.1017/S0022112005007160 Published online by Cambridge University Press

$e(p, v, \lambda)$ and $r(p, v, \lambda)$. An experimentally determined detonation normal shock velocity, shock curvature relationship and other experimentally determined responses such as the shock velocity as a function of a constant velocity piston impact, can be used to constrain the constitutive relations over a wide range of dynamically changing detonation states. Once defined, the constitutive description can be used in numerical modelling for multi-dimensional time-dependent simulations carried out with multi-material continuum mechanics based finite-element and finite-difference codes (i.e. hydrocodes) to make predictions beyond the scope of analytical description.

Thus, validation of theory by comparison with experiment has two valuable outcomes. First, a reduced dynamical description of the detonation front of the general form given by (1.1) can be developed. The DSD-motion rules replace the traditional Huygens construction to make improved engineering predictions for TOA of the detonation shock. The DSD motion rule can also calculate TOA for a detonation sub-scale model such as program burn, used in multi-material hydrocodes. (Program burn is an algorithm used in a multi-material hydrocode that uses pre-computed TOA to release the energy behind the detonation shock, Bdzil, Stewart & Jackson 2001; Kapila, Bdzil & Stewart 2004.) A second outcome is the generation of an equation of state and rate law pair required for direct (reactive burn) numerical simulation (DNS) that will precisely reproduce both the experimentally measured and the asymptotic form of the detonation shock velocity, curvature relation.

Bdzil and colleagues have mainly used rate stick experiments in PBX-9502 to develop a detonation velocity curvature relation for that explosive (Aslam, Bdzil & Hill 1998; Hill, Bdzil & Aslam 1998). In the rate stick experiment, the cylindrical charge is initiated in a stick that is long enough to establish a steady curved detonation travelling along the axis of the stick. The steady shape of the (assumed) axisymmetric shock is captured and the axial velocity and the shock shape, determines the normal to the shock and curvature on the shock as a function of the radial distance from the centreline, which in turn, determines the normal detonation shock velocity relation for that charge. By varying stick radii, we build up an extended D_n, κ relation. Hull (1993; 1997) carried out a different set of experiments that looked at the D_n, κ relation in the converging region for negative curvature, $\kappa < 0$. In these experiments, he ignited two spherical detonations from point detonations and let them collide.

Stewart, Davis & Yoo (2002) and Wescott, Stewart & Davis (2005) developed an EOS and rate law that can describe explosive behaviour over a wide range. Figure 1 shows the detonation velocity curvature relation calculated using this EOS/rate law pair with the method described in Stewart, Yao & Davis (2000) for the asymptotic theory. This $D_n - \kappa$ relation is the shock motion rule that is used here to compute the shock motion according to the reduced DSD description. Hull's (1993) D_n, κ relation based on his experimental data is also shown.

The assembly drawing of the DSD validation (passover) experiment used for this paper is shown in figure 2. A cylinder of PBX-9501 explosive (white material) has a disk of pure lead (grey object) embedded along the central axis. An initiation system starts a single hemispherical shaped wavefront that sweeps through the explosive from the bottom, then diffracts around the inert disk and finally exits the top plane of the charge. The time of the shock wave breakout across the top of the charge is recorded and to be compared to both the DSD and direct multi-material simulation. During the experiment, the detonation shock undergoes a change in topology as the single hemispherical shape is transformed into a toroid-shaped front as it diffracts about the embedded disk. This wave inversion process creates a wide range of states, and hence is a well-defined and challenging test of both the asymptotic theory and

https://doi.org/10.1017/S0022112005007160 Published online by Cambridge University Press

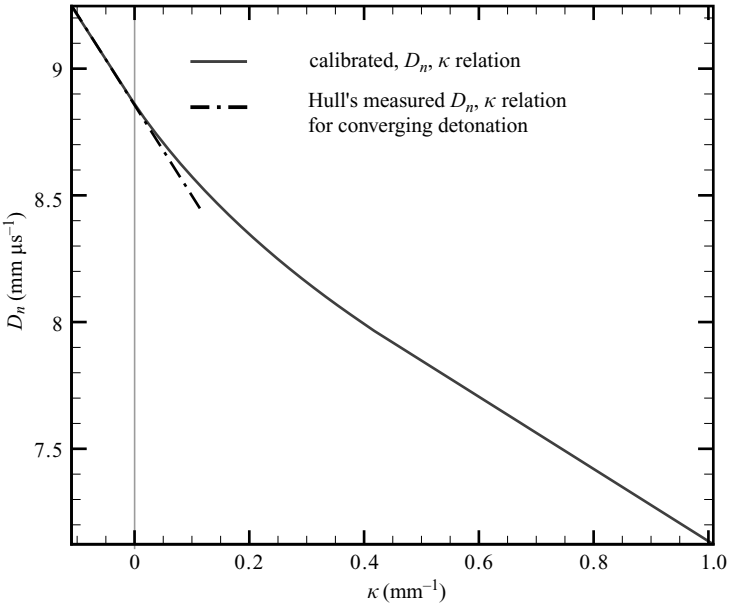


FIGURE 1. The D_n, κ relation for PBX-9501 calculated from the wide-ranging EOS and rate law model.

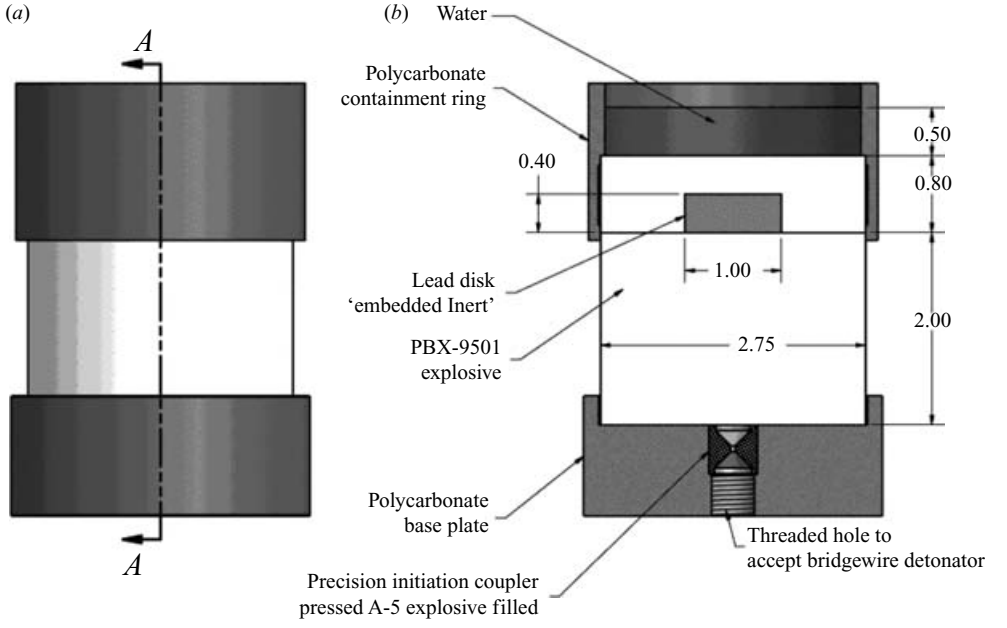


FIGURE 2. Assembly sketch for DSD validation experiment. (*b*) section *A*–*A*, scale 1:1, units in inches.

the numerical simulation. Figure 3 shows this sequence, as computed from DSD-theory.

In the sections that follow, we present the constitutive descriptions used to describe PBX-9501, the equation of state and rate law. This is followed by a brief

https://doi.org/10.1017/S0022112005007160 Published online by Cambridge University Press

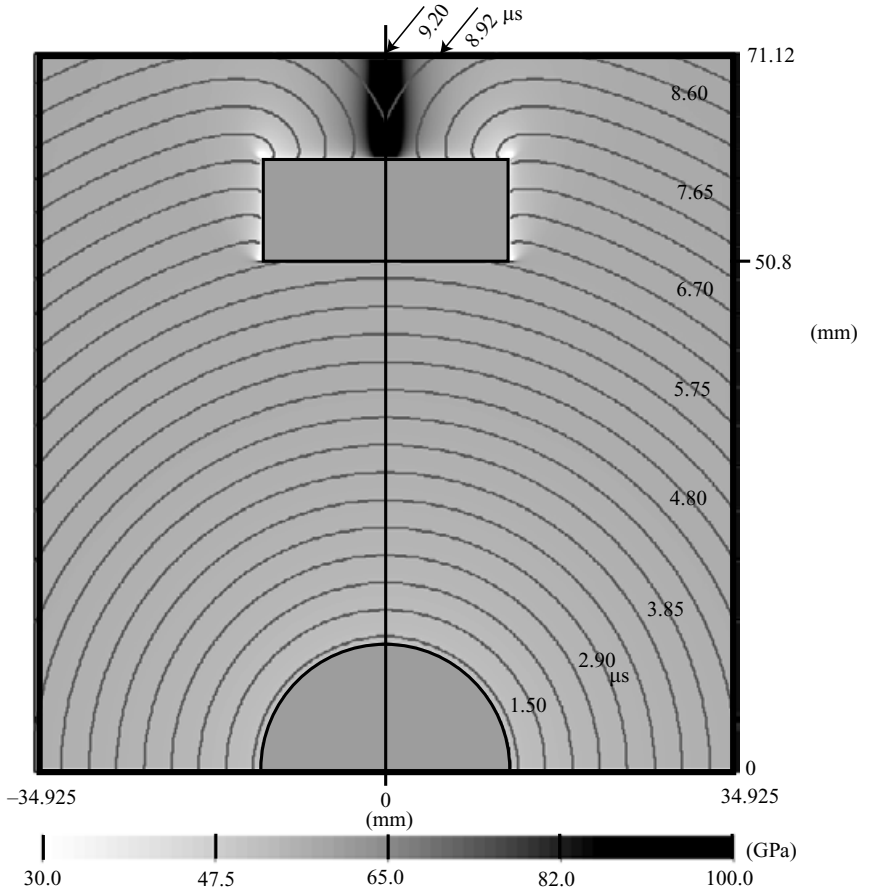


FIGURE 3. DSD simulation of the axisymmetric passover experiment. The grey-scaled plot shows the shock pressure in GPa when a shock passes a point (x, y) in the explosive. The labels on the curves show the location of the shock in μs. We see that the shock pressure around the lead disk is very low and is very high along the centreline over the lead disk. The shock pressure ranges from 50 to 70 GPa in most of the computational domain. The von Neumann spike for $D_n = D_{cj}$ is about 57 GPa.

description of the detonation shock dynamics computation that uses the motion rule and confinement angle. We then briefly describe the multi-material code used to simulate the 'passover' experiment. We give a complete description of the experiment. This is followed by a detailed comparison of the time of arrival compared against that obtained by the DSD simulation and the direct multi-material simulation. We conclude with a discussion of the agreement and discrepancies found between the experiment and the DSD and DNS simulation.

2. Constitutive description of PBX-9501 with the wide-ranging EOS and rate law

Davis (1985, 1993, 1998*b*) developed a wide ranging equation of state for detonation products whose form was chosen to describe accurately the physical behaviour of adiabatic γ (dimensionless sound speed) and Grüneisen gamma, Γ. Davis (2000) developed a similar reactants equations of state. Stewart *et al.* (2002) proposed a

https://doi.org/10.1017/S0022112005007160 Published online by Cambridge University Press

modification of Davis' reactant equation of state and introduced a closure model to develop a mixture EOS that includes the reaction progress variable of the form $e(p, v, \lambda)$ and that uses the standard rules for a binary mixture of reactants and products, where λ is the mass fraction of the products and is the reaction progress variable. Wescott *et al.* (2005) proposed a rate law for PBX-9502 that corresponds to rapid energy release near the shock, followed by a slower reaction in a longer tail. This work also used pressure–temperature equilibrium between the reactants and products. Shock to detonation data ('Pop'-plot) and detonation shock speed curvature data, were used to calibrate the parameters of the rate law. 'Pop-plots' named after Popolato (Gibbs & Popolato 1980) are log–log plots of an input shock pressure *vs.* the distance an inert shock travels before a self-sustaining detonation develops.

In all the works, the equation of state parameters were fitted to the shock Hugoniot data for both reactants and products. The calibration fit also included other considerations regarding the amount of usable work done by expanding gases for the products and consistent representations (and estimates) for the temperatures of the reactants and products. The methods used in the calibration are described in detail in Wescott *et al.* (2005).

Both reactants and products EOS are of the form $e(p, v)$,

$$e_p(p, v) = e^s(v) + \frac{v}{\Gamma_p(v)}(p - p^s(v)), \tag{2.1}$$

where e is the specific internal energy, and p and v are the pressure and specific volume, respectively. The quantities $e^s(v)$ and $p^s(v)$ are prescribed functions of v that are associated with reference states that are determined from experiment. The individual reactant and product phases are nominally described by their own pressure and specific volume denoted either by p_r, v_r or p_p, v_p. A mixture equation of state is defined by assuming a binary mixture of reactants and products with additive laws

$$e(p, v, \lambda) = (1 - \lambda)e_r(p_r, v_r) + \lambda e_p(p_p, v_p), \tag{2.2}$$

and

$$v = (1 - \lambda)v_r + \lambda v_p, \tag{2.3}$$

where the separate pressures are posited for the reactants and products. Closure requires two conditions which are taken to be pressure and temperature equilibrium as given between the reactants and products

$$p = p_r = p_p, \qquad T = T_r = T_p. \tag{2.4}$$

Other closure conditions can be considered, such as those described in Stewart *et al.* (2002), but pressure–temperature equilibrium is that most widely used in explosive modelling. Appendix A gives the specific wide-ranging fitting forms used for the reactant and products equations of states and the thermal properties that define the temperatures. Also, Appendix A includes the set of parameters used here to model PBX-9501.

Specifying separate EOS forms for the reactants and products combined with the closure conditions, gives a well-specified EOS of the general form $e(p, v, \lambda)$. Using the EOS for the products (by setting $\lambda = 1$) or the EOS for reactants (by setting $\lambda = 0$), the Rankine–Hugoniot relations can be applied to compute separate Hugoniot curves for comparison to experimental data. (The experimental data U_p–U_s in figures 4 and 5 cited in Stewart *et al.* (2002) was compiled by R. Gustavsen, Los Alamos National Laboratory and obtained via personal communication.) Figure 4 shows a plot of

https://doi.org/10.1017/S0022112005007160 Published online by Cambridge University Press

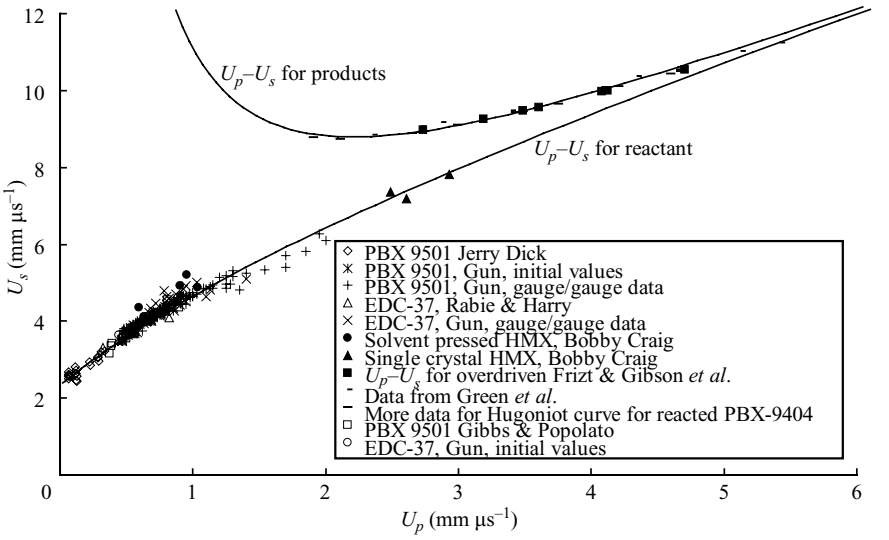


FIGURE 4. PBX 9501 $U_p - U_s$ Hugoniot and experimental data (Stewart *et al.* 2002).

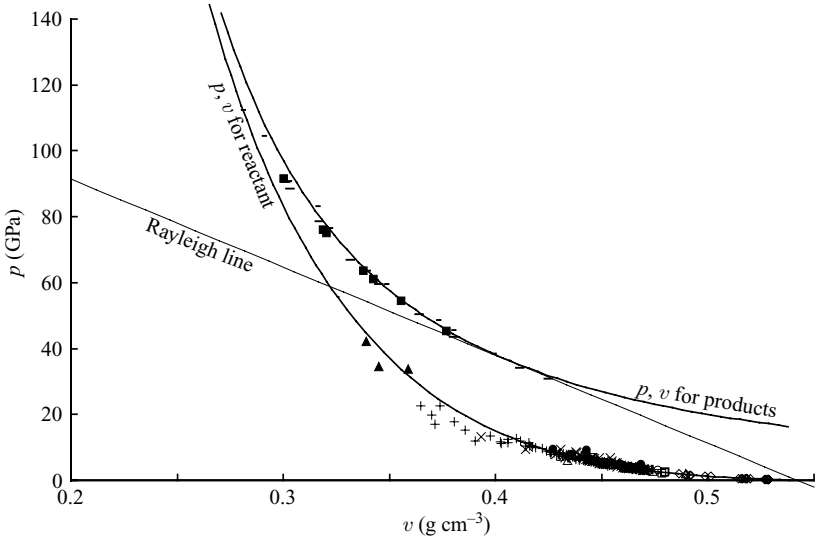


FIGURE 5. PBX-9501 p, v Hugoniot, Rayleigh line and experimental data (Stewart *et al.* 2002). See figure 4 for key.

the particle velocity, shock velocity (U_P, U_S) Hugoniot (top curve) calculated from the products EOS, and Hugoniot (bottom curve) calculated from the reactants EOS compared with experiment. Figure 5 shows the pressure, specific volume Hugoniot for the wide-ranging EOS compared against experiment.

3. Reaction rate law for PBX-9501

The Hull (1993) experimental data suggests the D_n, κ relation is linear near the CJ point. For this work we propose a single-term fractional depletion pressure-dependent

https://doi.org/10.1017/S0022112005007160 Published online by Cambridge University Press

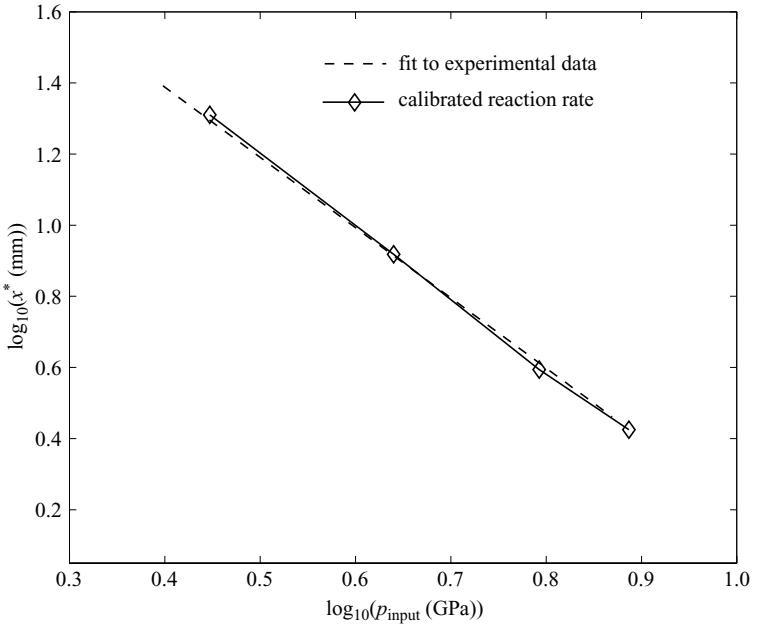


FIGURE 6. 'Pop'-plot, run to detonation distance versus input shock pressure (P_{input}) for PBX 9501 from Gibbs & Popolato (1980) and direct simulation results.

p_{CJ} (GPa)	k (μs^{-1})	N	ν
36.3	110	3.5	0.93

TABLE 1. Calibrated reactant parameters for PBX 9501.

reaction rate to model PBX-9501, of the form

$$r(p, v, \lambda) = k(1-\lambda)^{\nu}\left(\frac{P}{P_{CJ}}\right)^{N}. \tag{3.1}$$

The depletion exponent ν is picked primarily to match the slope of Hull's data, as indicated in figure 1. The pressure exponent N and rate constant k are adjusted to match the shock initiation ('Pop'-plot) data. One-dimensional reverse impact simulations were carried out using the specified EOS and rate law to match the published experimental data for PBX-9501, published in Gibbs & Popolato (1980), and the results shown in figure 6 show agreement over a wide range. The calibrated rate law parameters are shown in table 1.

4. The 'passover' experiment

The design of the passover experiment and the associated experimental technique is described in this section. The experiment provides a means to validate the simulations across a broad range of local wave curvatures. A limited calibration of the D_n, κ relation was generated from rate-stick and spherical wave interaction experiments as described in Hull (1997). The passover experiment is similar to the spherical wave interaction, but it is just different enough so that it can test the DSD, EOS/rate law

https://doi.org/10.1017/S0022112005007160 Published online by Cambridge University Press

models for material state regimes outside the calibrated domain in order to evaluate the robustness of the models.

The geometry and construction of the passover assembly, shown in figure 2, is intended to create a complex detonation shock structure using a relatively simple configuration geometry. The design allows a single quasi-steady hemispherical relatively unperturbed wave of convex curvature to be transformed into a half-ring torus-shaped wave shock with a region of high concavity at the central implosion axis.

4.1. *Detonation sequence*

A description of the sequence of events within the assembly is given. The entire apparatus is designed to maintain two-dimensional axial symmetry. The passover assembly consists of four significant components. The first is the main explosive charge of PBX-9501 comprised of two pieces: a lower solid cylinder of 69.85 mm (2.75 in) diameter by 50.8 mm (2.00 in) long and an upper cylinder of the same diameter, but with length 20.32 mm (0.80 in) and having a 25.4 mm (1.00 in) diameter cavity bored to a 10.16 mm (0.40 in) depth, centred on one end. The second component is a disk of pure lead, machined to fit the cavity in the top explosive piece. The third component is the polycarbonate hardware that physically holds the explosive cylinders together and holds the initiation system precisely at the centreline of the base charge. The initiation system is the fourth component of the experiment assembly. A precision initiation coupler (PIC) is located up against the base of the lower charge. It is a steel cylinder with an 'hour-glass' internal cavity that is press-filled with Composition A-5 explosive. The PIC is initiated by an explosive bridgewire detonator. Its purpose is to centre the detonation wave from the bridgewire detonator and to shape it into a more hemispherical geometry.

The selection of PBX-9501 was based on it being an explosive with existing DSD-characterization from Hull's previous work, it has been calibrated to the wide-ranging EOS and rate law of the previous section, and it can be pressed with excellent geometric tolerance and dimensional stability. The hardware used to attach the initiation assembly and align the top and bottom charges was designed to mimic a free-surface boundary (i.e. non-reflecting shock boundary) through minimal contact surface and the use of low-shock-impedance polycarbonate material. Pure lead was selected as the inert for its high shock-impedance and its well-characterized shock Hugoniot properties.

The detonation event begins at the bottom by firing the bridgewire initiator that ignites the PIC and, in turn, detonates the central base region of the PBX-9501 charge. The detonation shock front propagates through the explosive as a simply connected surface with convex positive curvature within the first 50 mm length of the PBX-9501 charge. The detonation then encounters the lead disk within the top piece of PBX-9501. The shock speed in the inert lead is much lower than the detonation velocity in the PBX-9501 and a diffraction event occurs as the detonation sweeps about the disk and encompasses it. The isochronal contour plot of figure 3 provides an excellent illustration of the motion of the detonation shock front as it sweeps around the lead disk.

The disk causes a 'doughnut' hole to be formed at the centreline of the top charge, hence, the half-ring torus-shaped front. The diffracted or retarded portions of the detonation progress towards the centreline and collapse the hole region. The colliding oblique shocks produce extraordinarily high pressures. As the centreline is closed, the shape becomes a half-horn torus which continues to progress in the axial direction and soon exits the top surface of the explosive cylinder. The column of water that sits

https://doi.org/10.1017/S0022112005007160 Published online by Cambridge University Press

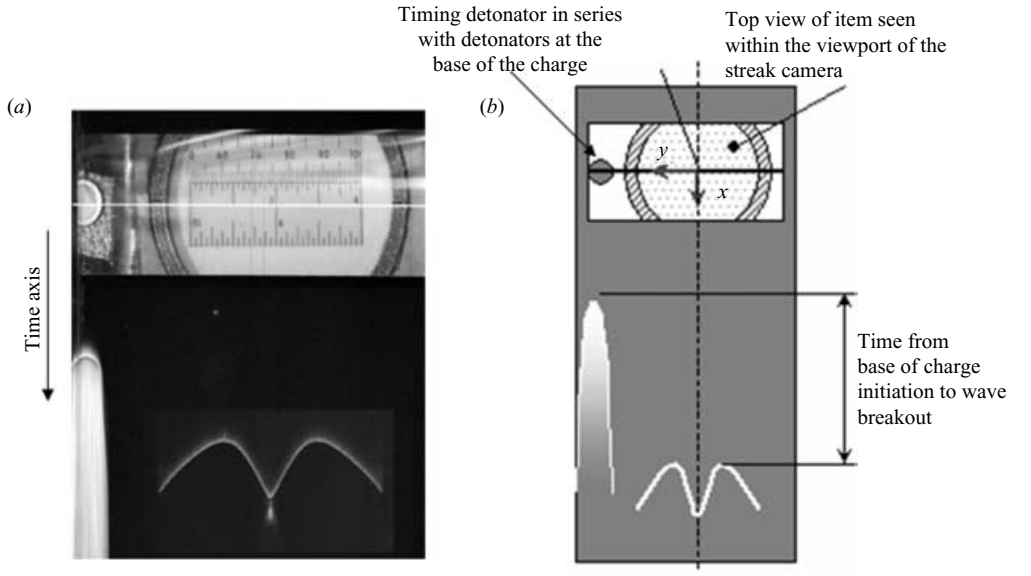


FIGURE 7. Streak camera results for passover experiments with view looking directly down on the cylinder through the water at the top surface of the explosives. (*b*) Definitions for the film records.

atop the charge extinguishes the reactive shock as it transmits into the non-reacting water. The explosive/water plane is the region of interest for recording the time-of-arrival of the detonation shock. Since the experimental design is axisymmetric, the numerical simulations can account for the exact geometry and the polycarbonate hardware.

4.2. *Instrumentation*

The primary experimental data is the time-of-arrival (TOA) of the detonation shock at a known location, which can be compared to the simulation data. A Cordin 132A smear (or streak) camera is used to measure the TOA by imaging a diametral line across the top surface, i.e. explosive/water interface. Photons emitted from the detonation reaction zone directly expose the photographic film. Photon emission abruptly ends as the reactive flow is truncated at the water interface. A single 150 μm slit aperture plate was used during the dynamic event. The Cordin 132A has a 70 mm wide film format for high spatial resolution. An example from one of the passover experiments is shown in figure 7 along with a description of the reference coordinates. The static image on the film – created using an open aperture before the dynamic event – shows a horizontal line across the mid-region that is where the slit views the experiment during streak imaging. The time axis progresses from top to bottom. The 'm'-shaped record is that generated from the horn-shaped reaction front intersecting the top plane of the explosive. The record shows (in a continuous time domain) the first intersection of the wave with the plane is in the region between that covered by the lead disk and outer charge wall.

A time reference fiducial for the initiation system is found by connecting two RP-1 bridgewire detonators (RISI Industries product) electrically in series. Each detonator had a PIC placed on top of it. One detonator/PIC system was inserted at the base of the explosive while the other was placed off to the side of the assembly, but oriented to allow the streak camera to view the output surface of the PIC. The RP-1s function

https://doi.org/10.1017/S0022112005007160 Published online by Cambridge University Press

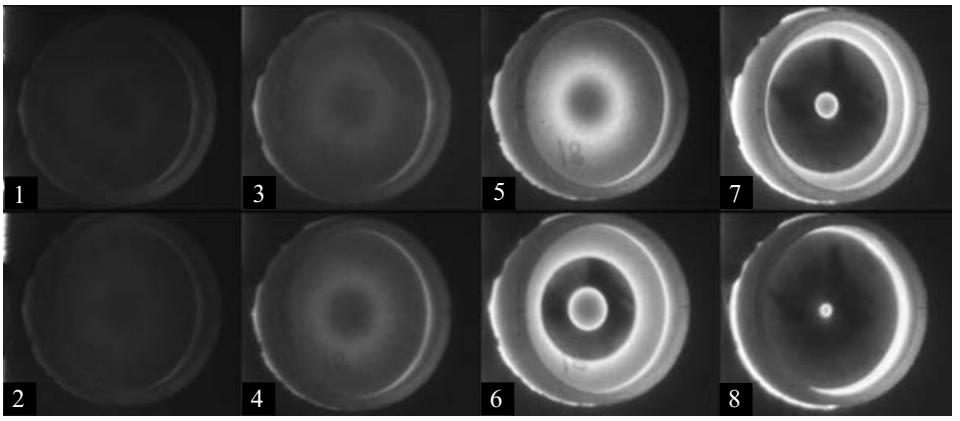


FIGURE 8. Framing camera sequence of a passover experiment.

within 25 ns of each other to give a total detonator/PIC system jitter of approximately 35 ns, considering PIC explosive pressing density variations and interface tolerances. This method established an optical fiducial on the film record and isolated the time it took for the detonation to traverse the entire length of the PBX-9501 charge, from the output of the PIC to the explosive/water interface. Now, the coordinate systems of the explosive and simulations can be precisely referenced. The explosive in the PIC had a 5 mm radius that was consistent with the initial shock radius assumed in the direct numerical simulations.

A total of four passover experiments were conducted with identical hardware. Each of the film records was digitized for TOA data to verify experimental precision. The records and their interpretation are presented in the next section along with the simulations. The imaging slit of 150 μm with a writing rate of 12 mm μs^{-1} presents an additional 12.5 ns of timing uncertainty in the film records. A total of approximately 47.5 ns uncertainty in the timing record can be accounted for from all sources when added to the bridgewire errors.

An Imacon 468 ultra-high-speed digital framing camera was also used to capture an overall view of the experiment. The framing camera captured the entire explosive diameter for several instances in time while the smear camera captured a slice (line) of the event for all time (continuous). The sequence of images in figure 8 is a framing counterpart to the corresponding streak image shown in figure 7. The Imacon is an image intensified camera with enough exposure sensitivity to capture the translucency of PBX-9501 as the detonation wave progresses through the charge. The series of images has a view that looks down at an angle slightly oblique to the top of the passover apparatus. The frames were taken with 150 ns inter-frame time with a 70 ns exposure duration. Frames 1 to 5 show illumination of the wave through the explosive charge. The wave is just about to exit the explosive/water surface in frame 5 while the leading part of the wave has already transmitted into the water in frame 6. Frames 7 and 8 show two distinct shock fronts intersecting the explosive's top surface: one that moves radially inward during the collapse of the torus' hole; and one of the torus body itself expanding radially outward.

These images capture the nearly instantaneous decomposition of solid phase to gas phase as the detonation wave sweeps the charge. They were all taken within a window of time before the high-pressure products had time to expand out physically and obscure the surface being viewed. Referring to frames 5–8, we find qualitative

https://doi.org/10.1017/S0022112005007160 Published online by Cambridge University Press

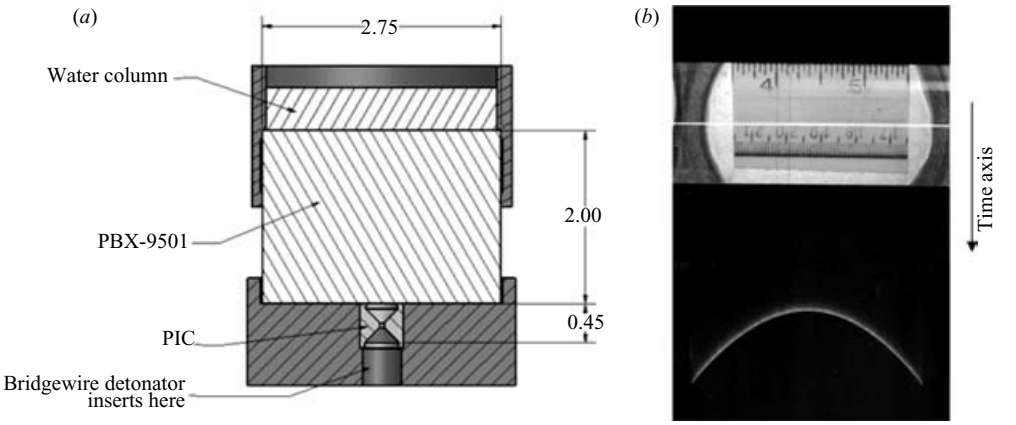


FIGURE 9. (*a*) Apparatus and (*b*) streak film for a single-point initiated cylinder.

appreciation for the extremely localized and diverse pressure states. The outward running detonation front separates material at pressure states of ambient, 10^{-5} GPa, just outside the front, but at (approximately) 35 GPa just inside it. In the centreline region, the pressure probably exceeds 50 GPa as the torus hole collides upon itself.

4.3. *An experiment without the embedded disk*

An experiment without the lead disk was conducted to establish the detonation wave shape just before encountering the lead disk. This was done to determine whether any discrepancies between the simulation and experiment were from multi-material boundary interactions or inadequate calibration of the models as the initially divergent wave transforms into a mixed curvature configuration. In other words, this experiment evaluates whether the simulation and the models match for the simplest case of a single expanding hemispherical front. This set-up simply removed the top 20.3 mm (0.80 in) piece of PBX-9501 and the lead disk with the containment ring with water sitting directly on top of just the 50.8 mm (2.00 in) charge. The apparatus for this experiment is given in figure 9 along with the streak film record. The film record shows the intersection of a single expanding hemispherical wave exiting a plane with the slit oriented along the diameter of the charge. The writing rate for this record was also 12 mm μs^{-1}. Corresponding Imacon images are found in figure 10. Each image is separated by 150 ns with a 70 ns exposure time. The leading part of the shock wave transfers from the explosive to the water between frames 3 and 4.

5. Description of the reduced (DSD) and direct multi-material numerical simulations (DNS)

Two different types of simulation were carried out to compare with the time of arrival results obtained by the passover experiments. The first is a simulation that uses the reduced DSD-model defined by the D_n, κ shock motion rule, subject to inert angle confinement boundary conditions. The mathematical formulation and a description of the level set method applied to detonation shock dynamics can be found in Aslam, Bdzil & Stewart (1996). The second is a multi-material simulation of the explosive interacting with the embedded lead disk. The explosive is described by the wide-ranging $e(p, v, \lambda)$ equation of state and rate law mentioned in the previous

https://doi.org/10.1017/S0022112005007160 Published online by Cambridge University Press

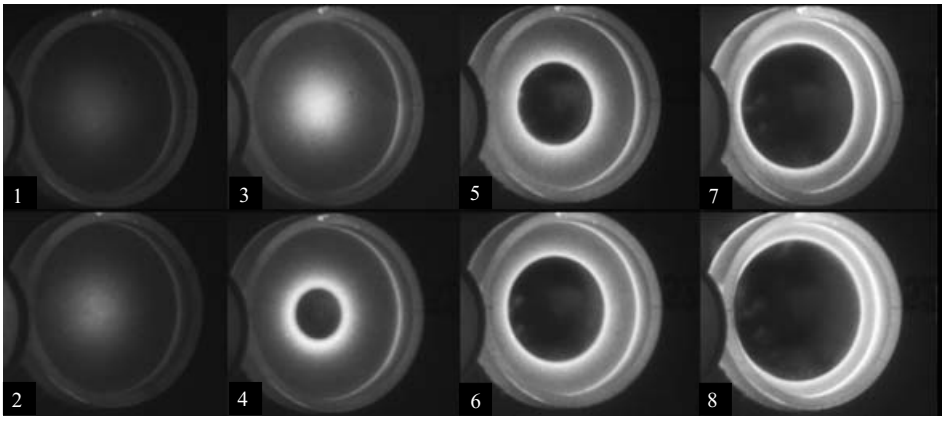


FIGURE 10. Framing camera sequence of a single-point initiated cylinder.

Material	ρ_0 (g cm^3)	c_0 (mm μs^{-1})	S	Γ_0
Lead (Pb)	11.35	2.05	1.46	2.8

TABLE 2. EOS parameters for lead.

sections and the lead disk is described by a Mie–Gruneisen EOS $e(p, v)$ of the form

$$e_{lead}(p, v) = \frac{v_o}{\Gamma_o}\left(p - \frac{c_o^2(v_o - v)}{[v_o - S(v_o - v)]^2}\right) + \frac{1}{2}\left(\frac{c_o(v_o - v)}{v_o - S(v_o - v)}\right)^2, \tag{5.1}$$

where we have used a standard assumption that Γ is linear in v with $\Gamma = \Gamma_0(v/v_0)$. The parameters for the lead EOS are given in table 2. The computational domain for both types of our simulations is $0 \leqslant x \leqslant 1.375$ in, $0 \leqslant y \leqslant 2.8$ in.

5.1. *DSD-based simulations*

A DSD simulation assumes that the detonation propagates according to (1.1), expressed for convenience as $D_n = D_{CJ}(1-\alpha(\kappa))$ where $\alpha(\kappa)$ is stored in an interpolant. The level-set method is a particularly effective way of carrying out accurate and coordinate free calculations of the detonation shock motions. Level sets were first used to calculate shock dynamics in Aslam *et al.* (1996). The specific algorithm implemented in this paper is a second generation hybrid level-set method that uses higher-order representations of fronts and is described in Yoo & Stewart (2005). For convenience, a DSD simulation may be referred to as 'WaveTracker' because of use of a WaveTracker code that has DSD-based motion rules in it. This will distinguish it from the multi-material direct numerical simulation that is termed a DNS simulation.

The shock locus must be given to compute the initial shock motion. Also, the angle that the normal of the detonation shock makes with the inert confining boundary is a prescribed function of the normal shock speed. The angle prescription depends on both the EOS of the explosive reactants and the inert material (see figure 11*a*). The detonation induces a shock in the inert and locally, near the shock intersection point, the flow can be assumed to be steady and governed by a local shock polar analysis that matches the states around the intersection point (Aslam & Bdzil 2002). Figure 11*b* shows the sonic and subsonic angles as functions of normal velocity D_n for a PBX-9501/lead pair, as computed with the EOS forms.

https://doi.org/10.1017/S0022112005007160 Published online by Cambridge University Press

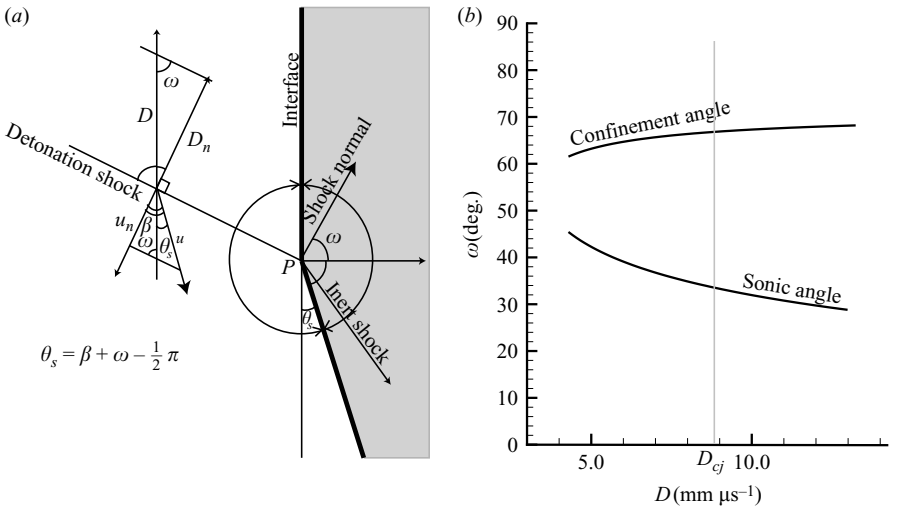


FIGURE 11. The detonation induces a shock in the inert and locally near the shock, at the shock intersection point P the flow can be assumed to be steady and governed by a local shock polar analysis that matches the states around the intersection point P. (*a*) The configuration of shock polar analysis. (*b*) Sonic and confinement angle for lead (Pb).

Figure 11(*b*) shows that at the point $D_n = D_{cj}$, the confinement angles are $\omega = 35°$(sonic) and 66°(subsonic). These angles are used for the boundary condition along the PBX-9501/lead interface. If the angle between the shock and the interface normals (e.g. ω in figure 11) is bigger than $\omega = 35°$(sonic), then the angle is enforced to be 66°(subsonic).

The initial shock in the DSD simulation is chosen to be a spherical shock of radius 5 mm centred at the bottom of the PBX-9501. This initial condition mimics the detonation that emerges into the PBX-9501 from initiation by the detonator/PIC system. The DSD simulation computes the shock motion and stores the shock TOA, D_n and other quantities at each grid point. Figure 3 displays a grey-scale colour contour plot of the shock pressure as the shock passes over points in the charge, and shock loci at uniform increments in time. At any point (x, y) in the charge in the rectangular computational domain, the level of grey scale at the point (x, y) shows the shock pressure when a shock passes the point, computed from the shock relations with the equation of state of the reactants for a given value of D_n. For reference, $D_{cj} = 8.86\,\text{mm}\,\mu\text{s}^{-1}$, the shock pressure $p = 58.87\,\text{GPa}$ and $v = 0.32\,(\text{g}\,\text{cm}^{-3})$ which is the von Neumann spike for PBX-9501.

5.2. *Direct multi-material numerical simulations (DNS)*

The direct multi-material numerical simulation for solving the Euler equations of the explosive coupled with those for the lead disk is summarized in this section. The explosive description uses the wide-ranging constitutive form described in the previous sections. The embedded lead disk is modelled with a standard Mie–Gruneisen EOS, given by (5.1). The external polycarbonate boundaries (Lexan) are not modelled directly, rather an outflow boundary condition is used. The multi-material simulation code combines two high-order solvers. A high-order total variation diminishing (TVD) solver is used for the Euler equations with the algorithms described in Xu, Aslam & Stewart (1997) for each material region (i.e. PBX-9501 and lead). The interface that

https://doi.org/10.1017/S0022112005007160 Published online by Cambridge University Press

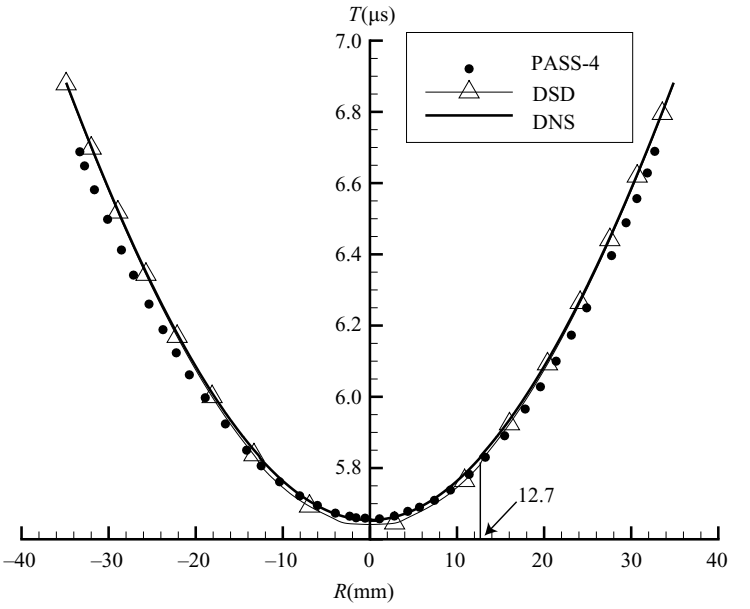


FIGURE 12. Time of arrival at the line $y = 50.8$ mm.

separates the different materials is represented by a zero level-set which in turn is embedded in a band of finite thickness. This band is used to update the position of the level contours in the band and hence advance the interface according to the normal particle velocity at the interface. In particular, the hybrid particle and level-set representation as described in Yoo & Stewart (2005) is used. The band is also used to extrapolate state values to either side to continue the material regions so that the material interface boundary conditions can be applied. Specifically, a Ghost Fluid Method described by Fedkiw *et al.* (1999) was modified for non-ideal EOS with a density extension and applied on the narrow-band domain around the moving interface. The resulting multi-material simulation is robust and has high accuracy when implemented on a Eulerian (fixed) grid. The full details of this implementation are documented in Stewart, Yoo & Wescott (2005).

For this numerical simulation, a spherical hot spot of radius 5 mm is located at the bottom in place of the PIC shown in figures 2 and 9. The pressure in the hot spot is 30 GPa the density 2.92 g cm^{-3}, is initially motionless and completely reacted. The boundary condition outside of the explosive material is continuous (outflow). Therefore, the DNS simulation uses an initial condition of a spherical detonation wave of radius $R = 5$ mm, assumed to have emanated from a point source at the centreline of the base.

6. Analysis and comparison of experiment and simulations

6.1. *Comparison and analysis of a simple divergent wave*

The (dotted) data in figure 12 labelled 'PASS-4' is the measured time of arrival at the top surface (height = 50.8 mm (2 in)) of the device for the experiment without the embedded disk as described in § 4.3. For comparison, figure 12 also displays the TOA at the top of the charge computed by the DSD-WaveTracker and the DNS

https://doi.org/10.1017/S0022112005007160 Published online by Cambridge University Press

simulation. The initial radius of shock for DSD simulation, both with and without the lead disk, was taken to be 12.7 mm (0.5 in). This value for the radius of the initial shock front was found to be sufficiently large that it was consistent with the DSD assumption that the flow is quasi-steady.

The TOAs generated from the DNS and DSD simulation were directly compared after making a time shift to account for the initiation transient such that the shock evolution simulated by the DNS was quasi-steady. In particular, the DNS simulation was computed from initiation by the 5 mm hot spot until the shock expanded to 12.7 mm, (which took 1.05 μs). From that point on, the DNS and DSD simulations were considered to be matched and allowed to proceed independently with no other modifications made as the simulations were carried out to completion. Then the TOA from the DNS simulation and the 'Pass-4' experiment were compared and an absolute time shift of 0.19 μs was used to match the experimental TOA data at the point of first arrival, as shown in figure 12. This time shift accounts for uncertainty and jitter of the absolute timing in the experiment and the differences between the initiation transient of the simulation and experiment.

Figure 12 shows that shapes of the DSD and DNS TOA data match each other and the experimental data to within an absolute difference of less that 0.03 μs in the entire region $0 \leqslant R \leqslant 34.952$ mm (2.75/2 in). Since the evolution takes place over an elapsed time of approximately 5.8 μs this represents a relative timing error for this region of less than 0.5 %. Over the entire top surface of the charge $0 \leqslant R \leqslant 34.952$ mm, the absolute time difference is less than 0.5 μs with a relative error of approximately 0.7 %. Part of the discrepancy might be attributed to a slight asymmetry in the experiment, as analysis of the experimental data indicates a non-smoothness (or inflection point) around $R = 20$ mm.

In order to estimate the effects of the transients that are found in the experiment, we made a comparison of the relationship between the measured normal detonation velocity and curvature as obtained from both the DSD simulation and DNS simulation. These were both compared against the theoretical (eigenvalue) D_n, κ relation that is obtained from the asymptotic theory. The shock position, normal velocity and shock curvature were recorded on a cone surface that corresponds to (i.e. a radial line emanating from the origin of the computational domain) the centre bottom of the main charge, oriented at an angle of 45°. Since the early evolution is essentially spherical, the shock curvature is simply computed as $2/R$ where R is the shock radius. Figure 13 shows the result of the comparison. In particular, at later times, the theoretical D_n, κ curve is attained by both the DSD and DNS simulations to a high degree. This agreement provides a check between the WaveTracker DSD simulation and the DNS. The DNS simulation shows evidence of an early transient. Starting from an initial hot spot radius of 5 mm the DNS simulation attains the theoretical quasi-steady D_n, κ curve in approximately 0.74 μs at about 10 mm. Some oscillation in the normal speed for the DNS can be attributed to the method of measurement of the DNS shock position. The shock position (i.e. shock crossing time) is recorded at each grid point the first time the pressure is larger than 1 GPa. Since the shock has a finite rise time that is about 4 computational cells thick, there is a corresponding first-order error, that is only diminished by increasing numerical resolution.

An assessment of the normal shock acceleration, $\dot{D}_n$, was conducted, shown in figure 18 and discussed in more detail in the next section. In particular, the value of $\dot{D}_n$ for the initial shock that emerges from the hot-spot initiation is one order of magnitude greater than that observed later as its radius increases along the centreline

https://doi.org/10.1017/S0022112005007160 Published online by Cambridge University Press

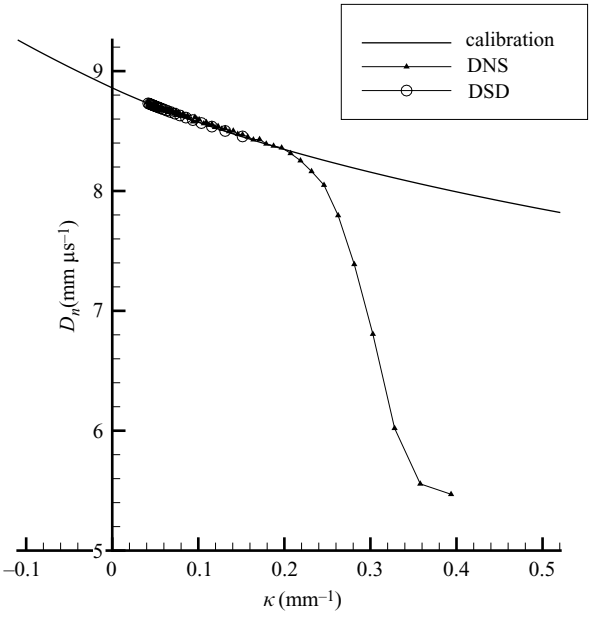


FIGURE 13. D_n, κ relations by calibration, DNS and DSD.

of the charge. This indicates that the shock evolves from the hot spot state to the quasi-steady state in a fairly short time.

6.2. *Comparison of DNS, DSD simulation and passover experiment*

Figure 14 shows a sequence obtained from a DNS simulation of the entire experiment, with the DSD-based shock superposed on the same plot. There is little observable discrepancy between the DSD shock location and the leading shock computed by DNS until the shock front turns around the upper corner of the lead disk. However, at the corners of the lead disk the effect of $\dot{D}_n$ is significant and the flow is more unsteady. The effects of higher-order transients are not included in the reduced DSD model (recall, only the D_n, κ relation is used) and so the mismatch of the DSD and DNS shock fronts in the top of the lead disk in figure 14 is understandable. There is a slight lag in the DNS as compared to the DSD in regions of negative shock curvature.

The sequence shown in figure 14 also demonstrates that the dimensions of the lead disk chosen for the passover experiment were appropriately chosen, since the time it takes for the shock to be transmitted through the disk is longer than the time it takes for the detonation to wrap around the disk. Hence, the simple DSD theory can be expected to be applicable to nearly all of the experimental TOA record measured at the top of the charge.

The flow unsteadiness is illustrated in the density record (figure 15*a*). The density of lead is 11.35 g cm^{-3} and the density of PBX-9501 is about 1.844 g cm^{-3} and is about 2.72 g cm^{-3} at the shock. Figure 15 (*b*) shows the progress variable λ ($\lambda = 1$ is burnt, $\lambda = 0$ is unburnt) around a corner at which the detonation shock turns. Observe the region of partial burning near the edge of the disk in the region that suffers large detonation diffraction as the detonation turns the corner. These regions are known to be associated with large relative pressure drops that in turn reduce the reaction rate. The one-dimensional Chapman–Jouguet reaction zone thickness for the equation of

https://doi.org/10.1017/S0022112005007160 Published online by Cambridge University Press

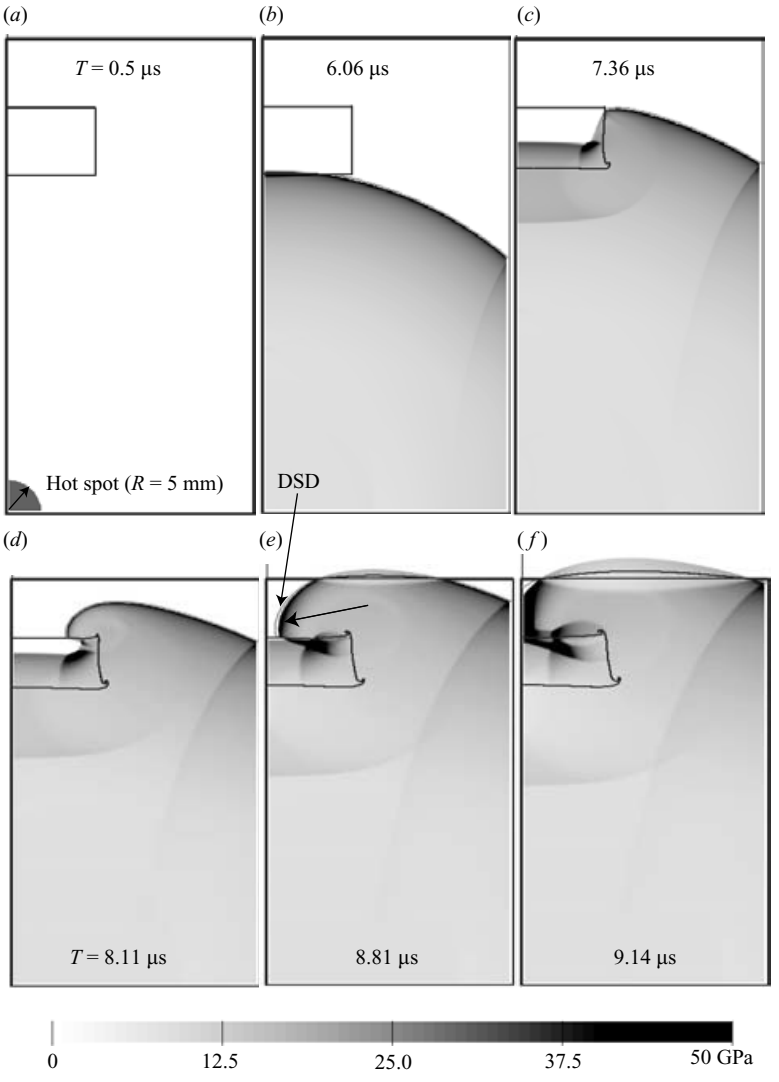


FIGURE 14. Comparison of DSD and DNS simulation. Shock front computed by DSD is overlapped on the pressure distribution computed by DNS at given time T. The shock front computed by DSD is shown by the dim curve as marked DSD in (e).

state and reaction rate assumed is 0.7 mm. In regard to numerical resolution for this analysis of reaction zone and the subsequent comparisons, the grid sizes $\mathrm{d}x = \mathrm{d}y$ are equally 0.0873 mm so that there are 400 grid points in the radial direction of the main charge. Therefore, we have nominally 8 to 10 points in the CJ reaction zone, but at speeds lower than D_{CJ}, the detonation reaction zone may have as many as 20 points.

Figure 16 is a composite of TOA records for the passover experiments that includes experiments, DSD simulations, DNS simulations and the ideal Huygens construction. Four experimental records are shown, labelled, 'Pass-1, Pass-2, Pass-3' and 'Pass-5'. Each set of experimental data is translated to match the time of first wave breakout because of small shot-to-shot jitter in the time that it takes for the initiation system response, (see figure 7). Once the fiducial time shift is made amongst the experiments,

https://doi.org/10.1017/S0022112005007160 Published online by Cambridge University Press

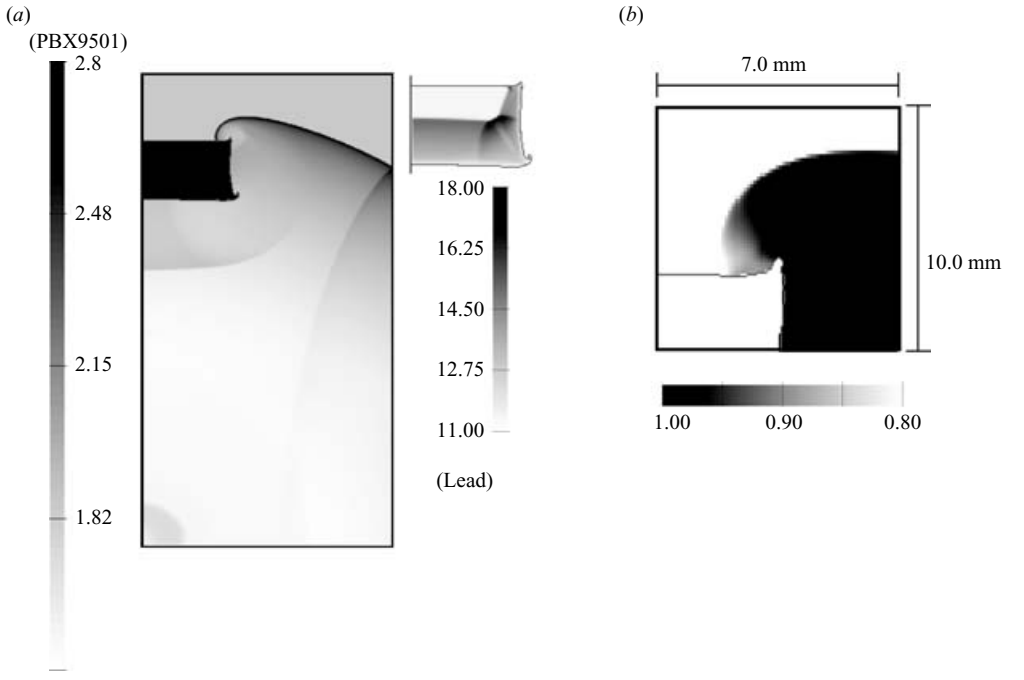


FIGURE 15. (*a*) The density field and (*b*) the progress variable λ at time $t = 7.79\,\mu s$. The density field of lead in the range $11 - 18\,g\,cm^{-3}$ is shown by an inset in (*a*). At the upper corner of the lead disk shown in (*b*), a vortex forms and there a dramatic decrease in the reaction rate as the pressure near the corner drops owing to the shock diffraction event.

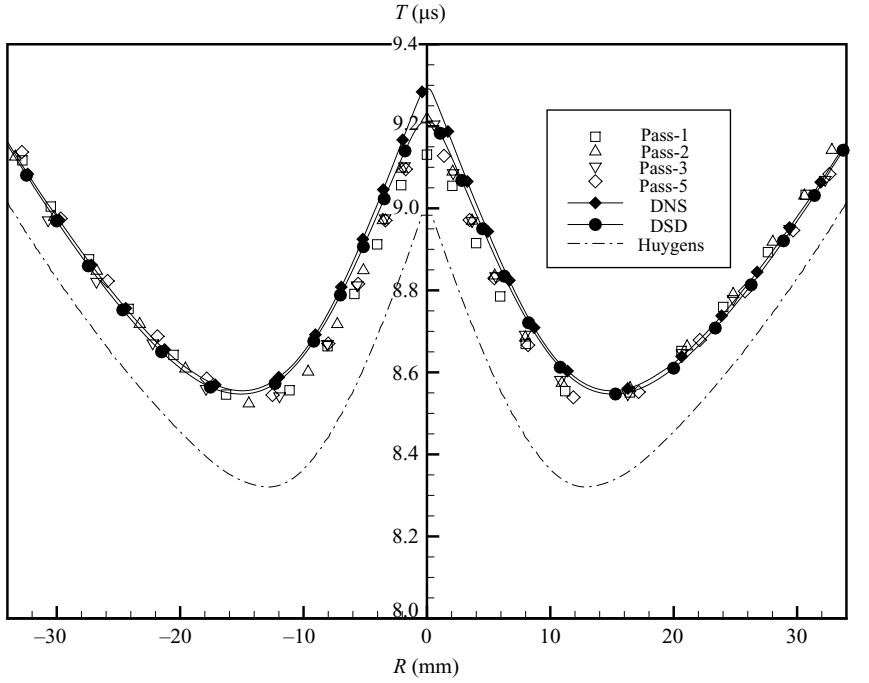


FIGURE 16. Passover comparison of experiments, DNS and DSD simulations.

https://doi.org/10.1017/S0022112005007160 Published online by Cambridge University Press

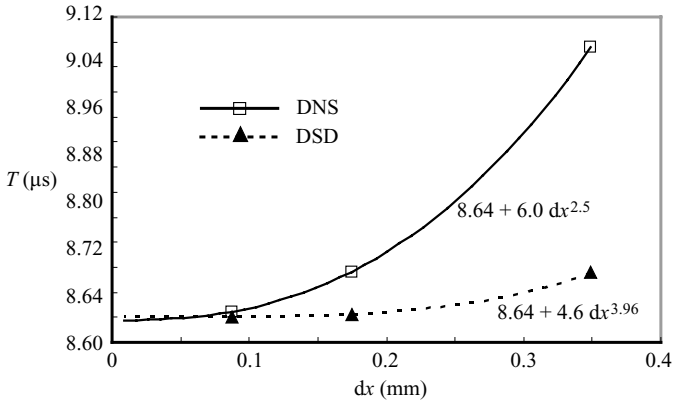


FIGURE 17. Convergence of TOA computation at $R = 10\,\text{mm}$.

the absolute time difference in these four independent experimental records is less than 0.3–0.5 μs, with the largest discrepancies in the region of convergence in the centre of the top of the charge. For comparisons of the DNS simulation and the experiments, Pass-1,2,3,5, a time shift of 0.5 μs was used to account for the initiation transient.

The TOA given by DSD matches the experimental data very well, but there is some discrepancy around the ordinate axis where the shock motion is affected by negative curvature (in the converging detonation) and where the unsteadiness of flow is significant, mainly around the corner of the lead disk. The largest discrepancy between the TOA of the DNS and the experiment is observed in the region $r \leqslant 2\,\text{mm}$, where the hole closes and the detonation shock topology become convergent. The explanation for the discrepancy between the DNS and the experiment may well rest in the need to include a change in the energy release mechanism for the explosive reaction zone when exposed to secondary shocks. The secondary shock (in this case provided by the primary shock collision that occurs with another portion of itself as the hole closes) causes a change in the material properties of the explosive particles in the pre-existing reaction zone and results in a change in the reaction rate. Our assumed form of the equation of state and rate law does not attempt to model this effect, or any other changes in the kinetics due to the occurrence of secondary shocks.

The DNS record for the TOA and the DSD record shown in figure 14 are nearly the same with an absolute time difference of less than 0.05 μs, except in the centre region. There, we do not expect the simple DSD theory to hold. The absolute time difference of the DSD and DNS records is less than 0.04 μs across most of the charge ($R > 2.5\,\text{mm}$, again except for the centre region where the difference is larger. This absolute time difference is at most approximately 0.4 % or less for approximately 92 % of the charge.

For the purpose of computing the shock time of arrival, the DSD simulation is an excellent alternative to the DNS simulation, since a DSD simulation usually requires 10 % or less time than does the corresponding DNS simulation with the same resolution. Also, the convergence rate of DNS computation with respect to the resolution is much slower than the corresponding DSD simulation. Figure 17 shows the convergence of a self-convergence test for the TOA at at fixed radius $R = 10\,\text{mm}$, for both the DNS and DSD simulations. The results suggest that DSD simulation converges more rapidly and a lower resolution simulation may be acceptable. In contrast, the DNS simulation converges much more slowly, since the DNS simulation

https://doi.org/10.1017/S0022112005007160 Published online by Cambridge University Press

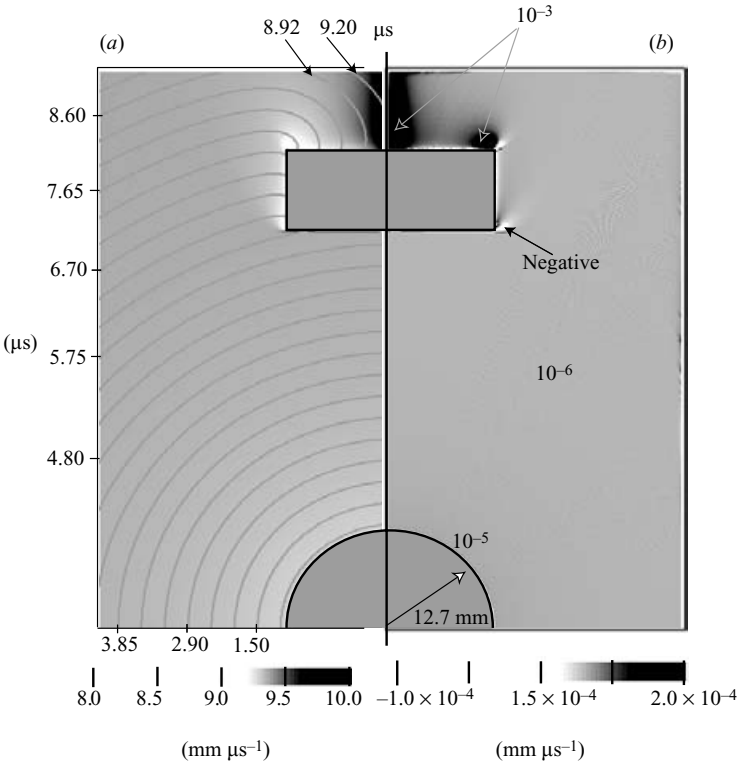


FIGURE 18. (*a*) Shock speed D_n and (*b*) $\dot{D}_n$ distributions. The left contour is the shock distribution on the computational domain with the TOA contour overlapped. $\dot{D}_n$ as a function of D_n in (*a*).

requires that the very thin reaction zone near the shock be adequately spatially resolved. Of the two, the DNS simulation is considered to be a more physically realistic simulation than the DSD simulation, but for comparable resolution, the DNS simulation takes a far longer time to compute than the DSD simulation.

Figure 16 shows the TOA obtained by a simulation of the detonation shock evolution according to a Huygens construction with an assumed constant normal shock speed of $D_{cj} = 8.86\,\text{mm}\,\mu\text{s}^{-1}$. The TOA at the top the surface is about 0.2 μs shorter than that obtained by the DSD/DNS predictions. This time difference is due to the accumulation of the curvature effect that slows the wave while the detonation propagates through the bulk of the charge. Adding the curvature effect to constant speed normal shock speed, i.e. D_n, κ model for DSD simulation, improves the prediction of the TOA significantly. We also observe a qualitative difference in the shape of the TOA record computed by the Huygens construction as compared to both the DSD and DNS simulation, owing to the absence of normal speed changes during the shock evolution governed by the Huygens construction. This leads us to assess systematically the effects of shock acceleration, $\dot{D}_n$ in the experiment.

A computed contour plot of the shock acceleration, $\dot{D}_n$ is shown in figure 18. Since we have found that the DSD and DNS simulations are nearly identical in most of the domain of the explosive, we made the following assumption. We assume that we can generate the correct TOA record from the DSD simulation, and from that record subsequently compute the shock location, the normal shock speed D_n and the normal

https://doi.org/10.1017/S0022112005007160 Published online by Cambridge University Press

shock acceleration $\dot{D}_n$. The advantage of using the DSD simulation to estimate shock acceleration is that the computed shock speed record is smoother. We could use the DNS directly, but the record for normal shock speed and, hence, acceleration is much noisier owing to the lower accuracy of the shock position. The formulae used to compute the normal shock speed D_n and acceleration $\dot{D}_n$ from the time of arrival (TOA) field are given in Appendix B. Figure 18 shows a side by side comparison of the DSD-computed shock positions (shown as solid lines in figure 18*a*), normal shock speed (shown as grey scale in figure 18*a*) and shock acceleration (shown as grey scale in figure 18*b*). We can immediately make some interesting observations. When the shock diffracts around the corners of the lead disk, the shock slows (with $\dot{D}_n < 0$) and then accelerates quite rapidly ($\dot{D}_n > 0$) once the shock has finished turning the corner. The diffraction is initially associated with a large rarefaction and the shock decelerates. Later, after the turn, the detonation feels the confinement and becomes subsonic at the edge, the reaction zone is re-pressurized and the shock accelerates to the quasi-steady state. This deceleration and re-acceleration is realized in the DSD-simulation through the imposition of the angle boundary condition. After the turn, the angle between shock normal and the interface normal becomes bigger than the sonic angle, so the shock is accelerated to make the angle equal to the confinement angle. This deceleration followed by acceleration is shown in figure 18 (*b*), the value $\dot{D}_n$ changes rapidly from negative (white) to positive (black).

In the converging region, above the upper right-hand corner of the lead disk, the effect of $\dot{D}_n$ is significant and unsteadiness of the flow appears prominent. Therefore, the difference between DSD simulation and DNS simulation is observed to be larger. To match the DSD shock evolution more accurately in the converging region, an extended model of DSD that includes higher-order transient effects must be used.

7. Conclusions

The passover experiment is an experiment that generates a large variation of the normal detonation velocity and produces a clear and reproducible experimental record (i.e. the TOA at the top surface of the charge). An appropriately sized lead disk is an excellent choice for the embedded object since it allows the detonation sufficient time before the transmitted shock is presented to unreacted explosive above the disk. The experiment can be designed such that there is little or no interference with evolution of the lead detonation shock, except for confinement in the interior of the charge. The wide-ranging equation of state and rate law was used to compute the simplest theoretically based D_n, κ relation that was then used for subsequent DSD-WaveTracker simulation of the shock motion. Also, that same constitutive description was used in a high-resolution multi-material code to carry out direct numerical simulation of the interaction of the explosive with the internal lead disk.

Excellent agreement between experiment, theory and direct multi-material simulation was achieved through careful analysis and understanding of the temporal and spatial relationships. Also, it was shown that the reaction zone effects were significant and must be included in order to achieve the level of validation with the experiments discussed here. This is very encouraging since PBX-9501 is widely considered to be an ideal explosive that is assumed to have small curvature effects. It was found that shock acceleration becomes important in areas of high diffraction and convergence. The level of agreement, both qualitative and quantitative, with experiment is encouraging because it indicates that we will be able to use descriptions like the wide ranging EOS/rate law and the corresponding reduced DSD description

https://doi.org/10.1017/S0022112005007160 Published online by Cambridge University Press

effectively to model real explosives and predict complex dynamic behaviors. The predictive requirements are dramatically increased as the application systems become more complex and/or smaller in size.

The work of D. S. S. and S. Y. at the University of Illinois was supported by grant (F08630-00-1-0002) from the Air Force Research Laboratory, Munitions Directorate. D. S. S. and B. L. W. were also supported by Los Alamos National Laboratory, DOE/LANL 3223501019Z. Los Alamos Report number LA-UR-05-0169.

Appendix A. Wide-ranging EOS description for PBX-9501

Equation of state for detonation products

A calibration procedure identical to that described in Wescott *et al.* (2005) was used to determine the model parameters for the wide-ranging rate law for PBX-9501. This calibration of the EOS of the products was described in (Davis 1985, 1993, 1998*b*) and Stewart *et al.* (2002) for PBX-9504 with the modification to the EOS as in Wescott *et al.* (2005). The equation of state for the products $e_p(p, v)$ is

$$e_p(p, v) = e_p^s(v) + \frac{v}{\Gamma_p(v)}\big(p - p_p^s(v)\big), \tag{A 1}$$

and

$$p(e_P, v) = p_p^s(v) + \frac{\Gamma_p(v)}{v}\big(e_p - E_p^s(v)\big). \tag{A 2}$$

where p is the pressure, e_p the specific internal energy, v the specific volume, and for the products, the superscript s indicates the function is defined at the point passing through the Chapman–Jouguet (CJ) state (the principal isentrope). From Davis (1993), the fitting forms are given by

$$p_p^s(v) = p_c \frac{\left[\frac{1}{2}(v/v_c)^n + \frac{1}{2}(v/v_c)^{-n}\right]^{a/n}}{(v/v_c)^{k+a}} \times \frac{k - 1 + F(v)}{k - 1 + a}, \tag{A 3}$$

$$F(v) = \frac{2a(v/v_c)^{-n}}{(v/v_c)^n + (v/v_c)^{-n}}, \tag{A 4}$$

$$\Gamma_p(v) = k - 1 + (1 - b)F(v), \tag{A 5}$$

$$e_p^s(v) = E_c \frac{\left[\frac{1}{2}(v/v_c)^n + \frac{1}{2}(v/v_c)^{-n}\right]^{a/n}}{(v/v_c)^{k-1+a}}, \tag{A 6}$$

$$E_c = \frac{p_c v_c}{k - 1 + a}. \tag{A 7}$$

where p_c, v_c, a, k, n and b are calibrated by fits to the experimental data as summarized in Wescott *et al.* (2005). Overall, three sets of parameters for the products EOS are identified as prescribed (from measurement), derived (to ensure consistent Chapman–Jouguet states) and calibrated. The set of parameters used for PBX-9501 are given in tables 3 and 4.

Using the EOS for the products, we can invoke the Rankine–Hugoniot relations to compute the Chapman–Jouguet end states. In particular, the CJ specific volume and the value of adiabatic gamma (the dimensionless sound speed) are found to be $v_{cj} = 0.4065\,(\mathrm{cm}^3\,\mathrm{g}^{-1})$ and $\gamma_{cj} = (c^2/(pv))_{CJ} = 2.992$, respectively. The temperature of the

https://doi.org/10.1017/S0022112005007160 Published online by Cambridge University Press

D_{cj} (mm μs^{-1})	p_{cj} (GPa)	ρ_o (g cm^{-3})	E_o (kJ/g)	k
8.86	36.3	1.844	5.85	1.3

TABLE 3. Measured PBX-9501 products parameters.

a	n	v_c (cm^3 g^{-1})	p_c (GPa)	b
0.7965	1.758	0.8314	3.738	0.7

TABLE 4. Calibrated PBX-9501 products parameters.

detonation products is used in the pressure–temperature closure rule for the mixture equation of state. Therefore, estimates for the temperature of the detonation products are required. The wide-ranging EOS is a complete EOS, with temperature given by

$$T_p(e_p, v) = T_p^s(v) + \frac{e_p - E_p^s(v)}{C_{v_p}}, \tag{A 8}$$

where the temperature on the principal isentrope is

$$T_p^s(v) = T_c \frac{\left[\frac{1}{2}(v/v_c)^n + \frac{1}{2}(v/v_c)^{-n}\right]^{(a/n)(1-b)}}{(v/v_c)^{k-1+a(1-b)}}, \tag{A 9}$$

$$T_c = \frac{2^{-ab/n}}{k-1+a} \frac{p_c v_c}{C_{v_p}}, \tag{A 10}$$

and where the specific heat of the products is estimated to be $C_{v_p} = 945\,\mathrm{J\,kg^{-1}\,K^{-1}}$.

Reactants EOS

The EOS for reactant (designated with an r subscript) takes the form

$$e_r(p, v) = e_r^s(v) + \frac{v}{\Gamma_r(v)}\big(p - p_r^s(v)\big), \tag{A 11}$$

$$p_r(e_r, v) = p_r^s(v) + \frac{\Gamma_r(v)}{v}\big(e_r - E_r^s(v)\big), \tag{A 12}$$

where the pressure on the principal isentrope for the reactants is

$$p_r^s(v) = \hat{p}\left[\sum_{j=1}^{3} \frac{(4By)^j}{j!} + C\frac{(4By)^4}{4!} + \frac{y^2}{(1-y)^4}\right], \tag{A 13}$$

with $y = 1 - v/v_o$ and $\hat{p} = \rho_o A^2/4B$, where A and B are determined from experimental shock Hugoniot data. Further,

$$e_r^s(v) = v_o \int_0^y p_r^s(\bar{y})\,\mathrm{d}\bar{y} + e_o, \tag{A 14}$$

$$\Gamma_r(y) = \Gamma_r^o + Zy, \tag{A 15}$$

$$\Gamma_r^o = \beta c_o^2/C_p, \tag{A 16}$$

$$Z = \big(\Gamma_{sc} - \Gamma_r^o\big)/y_{max}, \tag{A 17}$$

$$y_{max} = \frac{2}{\Gamma_p(y_{max}) + 2}, \tag{A 18}$$

https://doi.org/10.1017/S0022112005007160 Published online by Cambridge University Press

A (mm μs^{-1})	B	C	Γ_r^o	Z
2.339	2.737	1.45	0.7989	−0.03076

TABLE 5. Calibrated reactant parameters for PBX 9501.

where $\Gamma_{sc} = \Gamma_p(y_{max})$ guarantees that the shock compression limit for the products is the same as the reactants. Also, $\beta = 165 \times 10^{-6}\,\mathrm{K}^{-1}$ is the thermal expansion coefficient, $C_p = 1130\,\mathrm{J\,kg^{-1}\,K^{-1}}$ the specific heat at constant pressure, and $c_o = 2.339\,\mathrm{km\,s^{-1}}$ the bulk sound speed. Like the products EOS, the reactant EOS is calibrated against the experimental shock Hugoniot data (Stewart *et al.* 2002). The detailed procedures for this calibration are described in Wescott *et al.* (2005) and the EOS parameters of the reactants are shown in table 5. The U_p, U_s Hugoniot compared to experiment are shown in figure 4.

Since temperature equilibrium between products and reactants is used for closure of a mixture EOS, it is required to provide an estimate for the temperature of the reactants as well. The reactant temperature $T_r(E, v)$ is defined by the formula

$$T_r(E, v) = T_r^s(v)\left\{\frac{1+\alpha}{C_v^o T_r^s(v)}\left(E - E_r^s(v)\right) + 1\right\}^{1/(1+\alpha)}. \tag{A 19}$$

where the reactant temperature on the reference isentrope is

$$T_r^s(v) = T_o e^{-Zy}\left(\frac{v}{v_o}\right)^{-(\Gamma_r^o + Z)}, \tag{A 20}$$

where $T_o = 293\,\mathrm{K}$. The specific heat at constant volume is assumed to have a linear dependence on ΔS as in Davis (2004), and α measures variation of the specific heat at constant volume of the reactant with entropy for the reactants as given by $C_v = C_v^o + \alpha_r(S - S^s)$. For the reactants C_v^o is obtained from the thermodynamic relationship $C_v = C_p(1 + \beta\Gamma T)^{-1}$ with $C_v^o = 1088 J/kg$ at $T = 293K$. The constant α is determined as in Davis (2000) by estimating a temperature from a specified point on the reference isentrope. For the choice of a shock temperature chosen to be $T_N = 1800\,\mathrm{K}$, the value of $\alpha = 0.9644$.

Mixture EOS

The mixture equation of state is defined assuming a binary mixture of reactants and products that obey the additive rules

$$e(p, v, \lambda) = (1-\lambda)e_r(p_r, v_r) + \lambda e_p(p_p, v_p), \quad v = (1-\lambda)v_r + \lambda v_p, \tag{A 21}$$

where the separate pressures are initially positive for the reactants and products. Pressure and temperature equilibrium between the phases

$$p = p_r = p_p, \quad T = T_r = T_p. \tag{A 22}$$

is assumed for the closure conditions.

Appendix B. Computation of acceleration for a moving front

We consider the motion of a front described by a level set $\psi(x, y, t) = 0$ for all $t > 0$, that is prescribed by the normal velocity to the front that obeys $\boldsymbol{D} = D_n \boldsymbol{n}$. The

https://doi.org/10.1017/S0022112005007160 Published online by Cambridge University Press

motion of the front is governed by the hyperbolic equation

$$\dot{\psi}(x, y, t) = \left(\frac{\partial}{\partial t} + D_n \boldsymbol{n} \cdot \nabla\right) \psi = 0, \tag{B 1}$$

where $\boldsymbol{n}$ is the normal vector to the front. Assume that the front generates a unique TOA field $T(x, y)$. Define a level set by $\psi(x, y, t) = T(x, y) - t$. For any time specified t_0, $\psi(x, y, t_0)$ correspond to the zero level set contour or surface. The total time derivative is

$$\dot{\psi}(x, y, t) = \left(\frac{\partial}{\partial t} + D_n \boldsymbol{n} \cdot \nabla\right) \psi = -1 + D_n \boldsymbol{n} \cdot \nabla \psi = -1 + D_n |\nabla \psi| = 0. \tag{B 2}$$

Since $\nabla \psi = \nabla T$, it follows that

$$D_n = \frac{1}{|\nabla T|}. \tag{B 3}$$

Since $\partial D_n / \partial t = 0$ from (B 3), the time derivative of $\dot{D}_n$ is given by the simple formula

$$\dot{D}_n = \left(\frac{\partial}{\partial t} + D_n \boldsymbol{n} \cdot \nabla\right) D_n = D_n \nabla D_n \cdot \boldsymbol{n}. \tag{B 4}$$

REFERENCES

Aslam, T., Bdzil, J. B., & Hill, L. 1998 Extensions to DSD theory: analysis of PBX 9502 rate stick data. *Proc. 11th Detonation Symp. Office of Naval Research ONR* 33300-5, *Snowmass, CO, 1998*, p. 21.

Aslam, T. D. & Bdzil, J. B. 2002 Numerical and theoretical investigations on detonation-inert Confinement Interactions. *Proc. 12th Intl Symp. on Detonation*, *Office of Naval Research, San Diego, CA*, ONR 333-05-2, pp. 483–488.

Aslam, T. D., Bdzil, J. B. & Stewart, D. S. 1996 Level set methods applied to modeling detonation shock dynamics. *J. Comput. Phys.* **126**, 390–409.

Bdzil, J. B. 2003 High-explosives performance. *Los Alamos Sci.* **28**, 96.

Bdzil, J. B., Aslam, T. D., Catanach, R. A., Hill, L. & Short, M. 2002 DSD front models: nonideal explosive detonation. *Proc. 12th Intl Detonation Symp.*, *Office of Naval Research, San Diego, CA*, ONR 333-05-2, pp. 409–417.

Bdzil, J. B. & Stewart, D. S. 1989 Modeling of two-dimensional detonation with detonation shock dynamics. *Phys of Fluids* A **1**, 1261–1267.

Bdzil, J. B., Stewart, D. S. & Jackson. T. L. 2001 Program burn algorithms based on detonation shock dynamics: discrete approximations of detonation flows with discontinuous front models. *J. Comput. Phys.* **174**, 870.

Davis, W. C. 1985 Equation of state for detonation products. *Proc. 8th Detonation Symp.* p. 785–795.

Davis, W. C. 1993 Equation of state for detonation products. *Proc.* 10*th Intl Symp. on Detonation*, pp. 369–376.

Davis, W. C. 1998*a* Introduction to explosives, Chap. 1, in *Explosive Effects and Applications* ed. Zukas & W. P Walter, Springer.

Davis, W. C. 1998*b* Equation of state for detonation products. *Proc. 11th Intl Symp. on Detonation*, pp. 303–308.

Davis, W. C. 2000 Complete equation of state for unreacted solid explosive. *Combust. Flame* **120**, 399–403.

Fedkiw, R. P., Aslam, T. D., Merriman, B. & Osher, S. J. 1999 A non-oscillatory Eulerian approach to interfaces in multimaterial flows (the ghost fluid method). *J. Comput. Phys.* **152** 457–492.

Gibbs, T. R. & Popolato, A. (ed.) 1980 *LASL Explosive Property Data.* University of California Press, Berkeley.

Hill, L. G., Bdzil, J. B & Aslam, T. D. 1998 Front curvature rate stick measurements and detonation shock dynamics calibration for PBX 9502 over a wide temperature range. *Proc.*

https://doi.org/10.1017/S0022112005007160 Published online by Cambridge University Press

11th Intl Detonation Symp. Office of Naval Research ONR 33300-*5, Snowmass, CO, 1998*, p. 1029.

Hull, L. M. 1993 Mach reflections of spherical detonation waves. *Proc.* 10*th Intl Symp. on Detonation*, *Office of Naval Research ONR 33395-12, Boston, 1993*, p. 11.

Hull, L. M. 1997 Detonation propagation and Mach stem formation in PBXN-9.*Los Alamos TR* LA-UR-97-3827.

Kapila, A. K., Bdzil, J. B. & Stewart, D. S. 2004 On the structure and accuracy of programmed burn. *Combust. Theor. Modeling* (to appear).

Stewart, D. S. 1998 The shock dynamics of multi-dimensional condensed and gas phase detonations. *Proc. Combust. Inst.* **27**, 2189–2205.

Stewart, D. S. & Bdzil, J. B. 1988 A lecture on 'Detonation shock dynamics'. Mathematical Modeling in Combustion Science. Lecture Notes in Physics, vol. 249, pp. 17–30. Springer.

Stewart, D. S., Davis, W. C. & Yoo S. 2002 Equation of state for modeling the detonation reaction zone *Proc. 12th Intl Symp. Detonation, Office of Naval Research San Diego CA*, ONR 333-05-2, pp. 624–631.

Stewart, D. S., Yao, J. & Davis W. C. 2000 Computation of shock acceleration effects on detonation shock dynamics for explosives described by general equation of state. *Proc. Combust. Inst.* **28**, 619–628.

Stewart D. S., Yoo, S. & Wescott, B. 2005 High-order numerical simulation and modeling of the interaction of energetic and inert materials. Preprint.

Wescott, B. L., Stewart, D. S. & Davis, W. C. 2005 Equation of state and reaction rate for condensed-phase explosives. *J. Appl. Phys.* **98**, 053514.

Xu, S., Aslam, T. D. & Stewart, D. S. 1997 High resolution numerical simulation of ideal and non-ideal compressible reacting flows with embedded internal boundaries. *Combust. Theory Modeling*, **1**, 113–142.

Yoo, S. & Stewart, D. S. 2005 A hybrid level-set method for modeling detonation and combustion problems in complex geometries. *Combust. Theory Model.* **9**, 219–254.

https://doi.org/10.1017/S0022112005007160 Published online by Cambridge University Press